

# Chiral discrimination by polarization singularities of single metal sphere

Shiqi Jia,<sup>1</sup> Jie Peng,<sup>1</sup> Yuqiong Cheng,<sup>1</sup> and Shubo Wang<sup>1,2,\*</sup>

<sup>1</sup>*Department of Physics, City University of Hong Kong, Hong Kong, China*

<sup>2</sup>*City University of Hong Kong Shenzhen Research Institute, Shenzhen, Guangdong 518057, China*

(Dated: August 3, 2021)

The practical applications of chiral discrimination are usually limited by the weak chiral response of enantiomers and the high complexity of detection methods. Here, we propose to use the C lines (i.e., lines of polarization singularities) emerged in light scattering by a metal sphere to detect the chirality of small chiral particles. Using full-wave numerical simulations and analytical multipole expansions, we determined the absorption dissymmetry of the chiral particles at different positions on the C lines and found that it can be much larger than that induced by circularly polarized plane wave excitation. We uncover that the large dissymmetry factor is attributed to the asymmetric absorption of electric and magnetic dipoles induced by the C lines. The results can generate novel methods of chiral discrimination and may find applications in optical manipulations, optical sensing, and chiral quantum optics.

## I. INTRODUCTION

Chirality is a universal property of symmetry in nature that plays important roles in physics, chemistry, and biology [1]. An object possesses chirality if it cannot be superimposed on its mirror image. A chiral particle and its mirror-imaged particle form a pair of enantiomers that can have dramatic different properties deriving from opposite chirality [2–7]. The detection/separation of different enantiomers, referred to as chiral discrimination, has long been a major interest due to important applications in various fields such as pharmaceutical industries [8, 9].

One widely used chiral discrimination technique is circular dichroism (CD) spectroscopy [1], which has been applied to detect chiral molecules [10], proteins [11], nanostructures [12] and so on. The CD is based on the differential absorption of enantiomers under left-circularly polarized (LCP) light and right-circularly polarized (RCP) light. It is typically orders of magnitude weaker than the usual absorption spectrum. This is because that CD requires the coupling between electric and magnetic dipoles [13], while the usual absorption only requires electric dipole and thus is the much stronger. To enhance the chiral signals and the sensitivity of chiral discrimination, various methods have been proposed, such as using the superchiral field of a standing wave [14], vector beams with strong longitudinal components [15], chiral microwave three-wave mixing [16], plasmonic nanostructures [17–22], and metasurfaces [23–26]. Photoexcitation circular dichroism was also shown to have orders of magnitude improvement on the sensitivity [27].

In this paper, we propose a new method of chiral discrimination by using the C lines emerged in light scattering by single metal sphere. The C lines correspond to the loci of polarization singularities at which light is purely circularly polarized and the orientation (semi-major axis) of the polarization ellipse is not well defined [28]. The C

lines have been theoretically studied in various systems including paraxial waves [29, 30], Gaussian beams [31], general 3D fields [32], and photonic structures [33]. Interestingly, they can also emerge in light scattering by simple small particles, where the C lines can extend from the near-field to the far-field region [34]. The C lines have been employed to construct novel topological structures of light fields including Mobius strip [35] and knots [36–40]. Here, we apply the C lines emerged in light scattering to detect chiral particles. By calculating the absorption dissymmetry factor of the chiral particles, we show that the C lines can provide much higher sensitivity than circular polarized plane waves. In contrast to conventional methods of chiral discrimination, our proposed method does not rely on the use of chiral structures or chiral excitations, and it only employs an achiral metal sphere excited by a linearly polarized light.

The paper is organized as follows. In Sec. II, we discuss the scattering properties of the metal sphere and the induced C lines, where two types of C lines are identified based on their multipole components. In Sec. III, we show the absorption property of a chiral particle located on the Type-I C line that is contributed by high-order multipoles. As a comparison, in Sec. IV, we show the absorption property of the chiral particle located on the Type-II C line that is dominated by electric dipole. In both two cases, we compare our numerical results with the analytical results of multipole expansions. We then draw the conclusion in Sec. V.

## II. THE C LINES OF A GOLD SPHERE

We consider a gold sphere under the excitation of a linearly polarized plane wave propagating in  $z$  direction and polarized in  $x$  direction. The radius of the sphere is  $r = 300$  nm. The relative permittivity of gold is described by a Drude model  $\epsilon_{\text{Au}} = 1 - \omega_p^2 / (\omega^2 + i\omega\gamma)$ , where the plasmonic frequency is  $\omega_p = 1.28 \times 10^{16}$  rad/s, and the damping frequency is  $\gamma = 7.10 \times 10^{13}$  rad/s [41]. To

\* shubwang@cityu.edu.hk

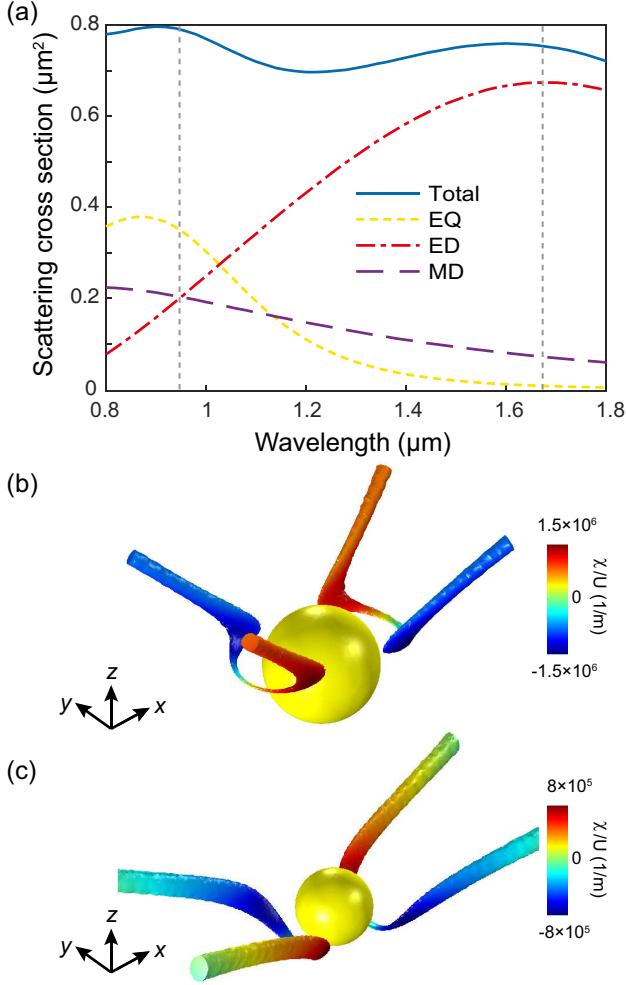


FIG. 1. (a) Scattering cross section of the gold sphere illuminated by a  $x$ -polarized plane wave propagating in  $z$  direction. (b) Type-I C line of the gold sphere at  $\lambda = 950$  nm. (c) Type-II C line of the gold sphere at  $\lambda = 1680$  nm. The color of the C lines denotes the normalized optical chirality  $\chi/U$ .

characterize the scattering property of the gold spherical particle, we first conduct full-wave simulations of the system by using COMSOL Multiphysics [42] and calculated the scattering cross section of the sphere. The result is denoted by the solid blue line in Fig. 1(a). We then decompose the scattering field of the sphere into electromagnetic multipoles as [43, 44]:

$$\mathbf{E}_s = E_0 \sum_{l=1}^{\infty} \sum_{m=-l}^l i^l [\pi(2l+1)]^{\frac{1}{2}} \left\{ \frac{1}{k} a_E(l, m) \nabla \times [h_l^{(1)}(kr) \mathbf{X}_{lm}(\theta, \phi)] + a_M(l, m) h_l^{(1)}(kr) \mathbf{X}_{lm}(\theta, \phi) \right\}, \quad (1)$$

where  $E_0$  is incident electric field amplitude,  $\mathbf{X}_{lm}$  and  $h_l^{(1)}$  are the normalized vector spherical harmonics and the spherical Hankel functions of the first kind, respectively. The vector functions  $\nabla \times [h_l^{(1)}(kr) \mathbf{X}_{lm}(\theta, \phi)]$  and  $h_l^{(1)}(kr) \mathbf{X}_{lm}(\theta, \phi)$  constitute a complete basis, where

each function of  $(l, m)$  describes the field contributed by a unique multipole. The integer  $l$  indicates the order of the multipole, and the integer  $m$  denotes the projection of the angular momentum along  $z$  axis. The multipole coefficients  $a_E(l, m)$  and  $a_M(l, m)$  characterize the weighting of the excited multipoles of the sphere, where the subscripts “E” and “M” distinguish between electric and magnetic multipoles. As for a known electric field  $\mathbf{E}(\mathbf{r})$  around the scatterer, the scattering current density is  $\mathbf{J}_s(\mathbf{r}) = -i\omega [\varepsilon(\mathbf{r}) - \varepsilon_h] \mathbf{E}(\mathbf{r})$ , where the  $\varepsilon(\mathbf{r})$  is the permittivity at an arbitrary point  $\mathbf{r}$ , and  $\varepsilon_h$  is the permittivity of the host medium. Using the Riccati-Bessel functions  $\psi_l(kr) = kr j_l(kr)$ , the multipole coefficients can be expressed as [45]:

$$a_E(l, m) = \frac{(-i)^{l-1} k^2 \eta O_{lm}}{E_0 [\pi(2l+1)]^{\frac{1}{2}}} \int \exp(-im\varphi) \left\{ [\psi_l(kr) + \psi_l''(kr)] P_l^m(\cos\theta) \hat{r} \cdot \mathbf{J}_s(\mathbf{r}) + \frac{\psi_l'(kr)}{kr} [\tau_{lm}(\theta) \hat{\theta} \cdot \mathbf{J}_s(\mathbf{r}) - i\pi_{lm}(\theta) \hat{\phi} \cdot \mathbf{J}_s(\mathbf{r})] \right\} d^3r, \quad (2)$$

$$a_M(l, m) = \frac{(-i)^{l+1} k^2 \eta O_{lm}}{E_0 [\pi(2l+1)]^{\frac{1}{2}}} \int \exp(-im\varphi) j_l(kr) \cdot \left[ i\pi_{lm}(\theta) \hat{\theta} \cdot \mathbf{J}_s(\mathbf{r}) + \tau_{lm}(\theta) \hat{\phi} \cdot \mathbf{J}_s(\mathbf{r}) \right] d^3r, \quad (3)$$

where  $P_l^m$  are associated Legendre polynomials,  $O_{lm} = [l(l+1)]^{-\frac{1}{2}} \left[ \frac{(2l+1)}{4\pi} \frac{(l-m)!}{(l+m)!} \right]^{\frac{1}{2}}$ ,  $\tau_{lm}(\theta) = dP_l^m(\cos\theta)/d\theta$  and  $\pi_{lm}(\theta) = mP_l^m(\cos\theta)/\sin\theta$ . We note that the multipole coefficients for a sphere can also be analytically obtained using Mie coefficients [43]. We implement the above numerical method in COMSOL for consistence with the visualization of C lines (to be discussed later). Using the above multipole coefficients, the total scattering cross section can be expressed as [43, 45]:

$$C_{\text{sca}} = \frac{\pi}{k^2} \sum_{l=1}^{\infty} \sum_{m=-l}^l (2l+1) (|a_E|^2 + |a_M|^2). \quad (4)$$

Equation (4) can be employed to determine the contribution of individual multipole to the total scattering cross section. The contributions of the electric dipole, the magnetic dipole and the electric quadrupole are shown in Fig. 1(a) as the dot-dashed red line, the dashed purple line, and the dashed yellow line. We will focus on the C lines of the electric field at two wavelengths  $\lambda = 950$  nm and  $\lambda = 1680$  nm, which are referred to as Type-I C line and Type-II C line, respectively. For the Type-I C line, the electric dipole, the magnetic dipole, and the electric quadrupole all contribute significantly to total scattering cross section, while for the Type-II C line the scattering cross section is dominated by the electric dipole moment.

The C lines can be directly visualized in COMSOL by determining the phase singularities of the scalar field  $\Psi = \mathbf{E} \cdot \mathbf{E}$  [34], and the results are shown in Fig. 1(b) and (c) for Type-I and Type-II C lines, respectively. We

notice that the C lines have similar structures in these two cases, i.e., a pair of C lines emerges in the near field and extends to the far-field region. To characterize the properties of the C lines for chiral discrimination, we then calculate the optical chirality of the C lines as [14]:

$$\chi = \frac{\epsilon_0}{2} \mathbf{E} \cdot \nabla \times \mathbf{E} + \frac{1}{2\mu_0} \mathbf{B} \cdot \nabla \times \mathbf{B}. \quad (5)$$

The ratio of  $\chi$  and the total field energy density  $U$  determines the degree of chiral asymmetry in the rate of excitation of a small chiral particle. The color of C lines in Fig. 1(b) and (c) shows the value of  $\chi/U$ . We notice that  $\chi/U$  is larger in the near field and its sign varies on the same C line. In addition, the value of  $\chi/U$  is larger for the Type-I C line that has significant contribution from higher-order multipoles.

### III. ABSORPTION OF A CHIRAL PARTICLE AT THE TYPE-I C LINE

We first consider the absorption of a chiral particle locating at the Type-I C line, as shown in Fig. 2(a). Due to the symmetry of the C lines, we only consider one of the C lines in Fig. 1(b). The chiral particle is a two-pitch gold helix with minor radius  $r = 5$  nm, major radius  $R = 10$  nm, and pitch  $p = 15$  nm, as shown in the inset in Fig. 2(a). We study the absorption of the chiral particle while it moves along the C line (with center axis aligned in the  $x$  direction), and totally 11 positions as marked by the black dots in Fig. 2(a) are considered.

We numerically calculated the normalized absorption cross sections (ACS) of the left-handed (LH) and right-handed (RH) helices. The results are denoted as the solid-blue line and dashed-red line in Fig. 2(b), respectively. The ACS of LH helix reaches the maximum and minimum at the positions 4 and 8, respectively, while the ACS of the RH helix shows an opposite trend. At the center position 6 where  $\chi/U$  vanishes, the LH and RH helices give rise to equal ACS as expected. To characterize the difference in response of LH and RH helices to the C line, we define the dissymmetry factor as [14]:

$$g = \frac{2(C_{\text{abs}}^+ - C_{\text{abs}}^-)}{C_{\text{abs}}^+ + C_{\text{abs}}^-}, \quad (6)$$

where  $C_{\text{abs}}^+$  ( $C_{\text{abs}}^-$ ) is the absorption cross section of LH (RH) helix. The numerical results of  $g$  (red dashed line) and the ratio  $\chi/U$  (blue line) are shown in Fig. 2(c). As seen, the dissymmetry factor  $g$  reaches +1 and -1 at the positions 4 and 8 respectively, which are much larger than that under the excitation of a circularly polarized plane wave at the same wavelength ( $g = 0.28$  for the considered helix particle). The position of the maximum/minimum of  $g$  as well as its trend agree with the ratio  $\chi/U$ . This indicates that the asymmetry of absorption is roughly proportional to the normalized optical chirality.

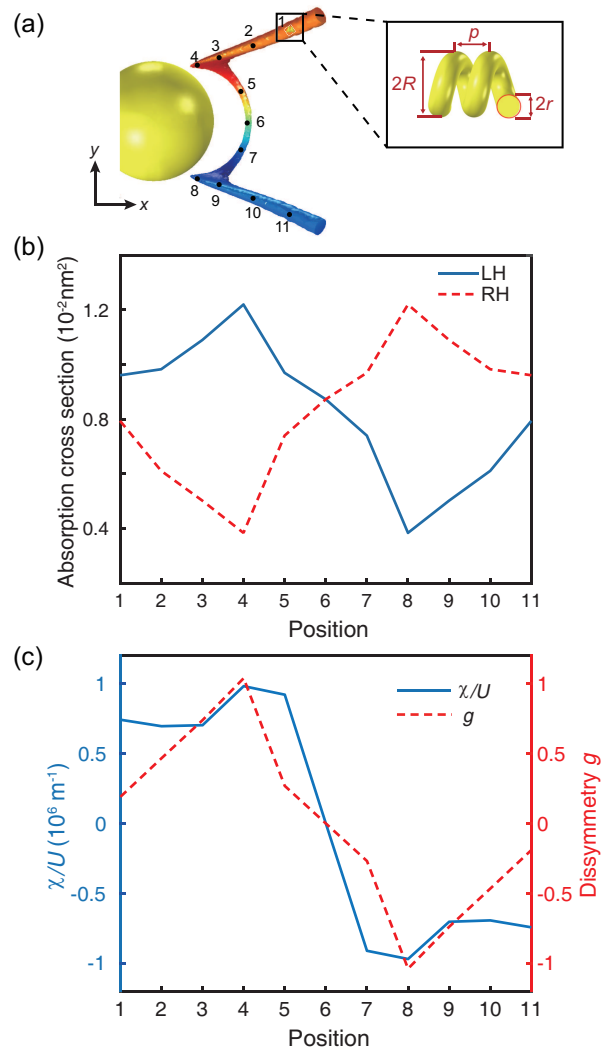


FIG. 2. (a) Schematic for chiral discrimination by the Type-I C line. A two-pitch gold helix serves as the chiral particle and is located at the positions labeled as 1-11. Its inner radius  $r = 5$  nm, outer radius  $R = 10$  nm, pitch  $p = 15$  nm. (b) The absorption cross section of the LH (blue line) and RH (red line) helices as a function of the position. (c) The dissymmetry (blue line) and the normalized optical chirality (red line) as a function of the helix's position.

To obtain intuitive understanding of the above numerical results, we apply multipole expansions to the helix particle and treat it approximately as a superposition of electric and magnetic dipoles due to the deep subwavelength of the particle size. Then, the total absorption of the particle can be evaluated as:

$$A^\pm = \frac{\omega}{2} \text{Im}(\mathbf{E}^* \cdot \mathbf{p} + \mathbf{B}^* \cdot \mathbf{m}), \quad (7)$$

where the Cartesian components of electric dipole moment  $\mathbf{p}$  and magnetic dipole moment  $\mathbf{m}$  are evaluated using  $p_i = -\frac{1}{i\omega} \int_V J_i dv$  and  $m_i = \frac{1}{2} \int_V (\mathbf{r} \times \mathbf{J})_i dv$  [4]. Fig. 3(a) and (b) shows the amplitudes of the electric

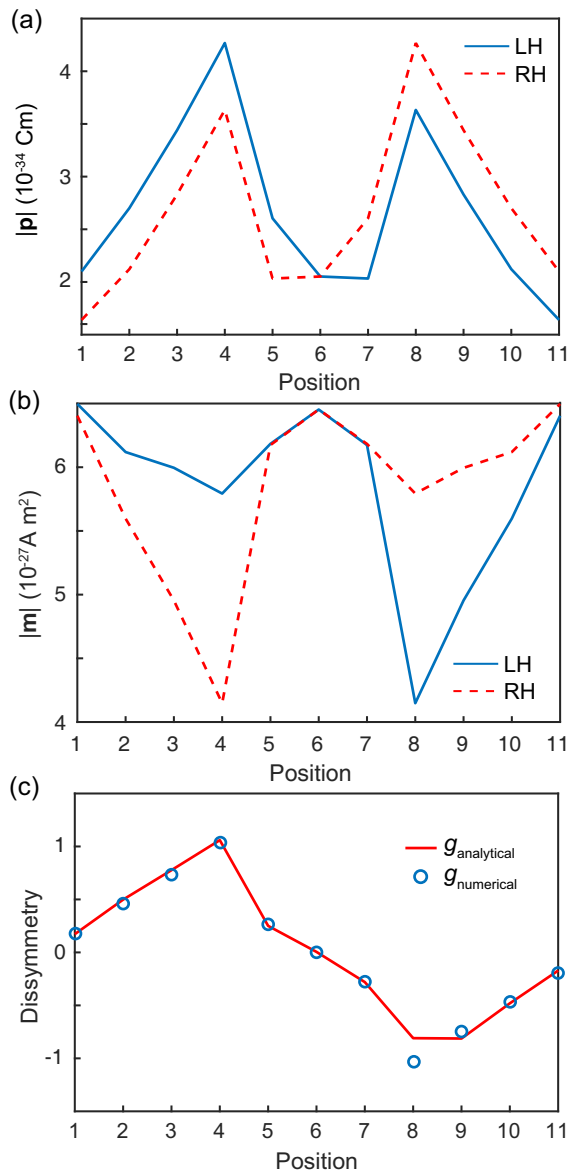


FIG. 3. Amplitude of (a) the electric dipole moment  $\mathbf{p}$  and (b) the magnetic dipole moment  $\mathbf{m}$  of the helices as a function of the position for the Type-I C line. (c) Comparison between the analytical (solid line) and numerical (symbol line) results of the dissymmetry factor.

and magnetic dipoles induced in the LH (blue line) and RH (red line) helices at the considered positions, respectively. We notice that the dipoles of LH and RH helices are mirror-symmetric with respect to the center position 6. In addition, for either helix particle, both  $|\mathbf{p}|$  and  $|\mathbf{m}|$  are asymmetric with respect to the center position 6 due to the chirality of the particle. Interestingly, at the positions 4 and 8,  $|\mathbf{p}|$  reaches local maximums, while  $|\mathbf{m}|$  reaches local minimums. We apply Eqs. (6) and (7) to analytically evaluate the absorption dissymmetry factor, and the result is shown in Fig. 3(c) as the solid line, which agrees well with the full-wave numerical result

(symbol line). This indicates that the absorption dissymmetry can be attributed to the difference of electric and magnetic dipoles induced in the chiral particles.

#### IV. ABSORPTION OF A CHIRAL PARTICLE AT THE TYPE-II C LINE

The Type-I C line is contributed by the electric dipole, magnetic dipole and electric quadrupole induced in the gold sphere. To understand how the different multipole components of a C line affects the optical chirality and the absorption of a chiral particle, we then consider the configuration in Fig. 4(a), where the helix particle locates at the Type-II C line that is dominated by electric dipole moment. Similarly, we calculated the ACS of the same LH and RH helices located as different positions of the C line, and the results are shown in Fig. 4(b). In contrast to the case of Type-I C line, the ACS of the helices are more symmetric in this case. The ACS of the LH helix reaches the minimum value at position 7, while the minimum ACS of the RH helix is at position 5.

We also calculated the normalized optical chirality  $\chi/U$  and the dissymmetry factor  $g$ , and the results are shown in Fig. 4(c) as the solid and dashed lines, respectively. Similar to the Type-I case, the sign of  $\chi/U$  changes at the center position 6 where the optical chirality vanishes. The result shows that the dissymmetry factor  $g$  is approximately proportional to the normalized optical chirality  $\chi/U$ . Notably, although  $\chi/U$  can reach  $\pm 1$ , the dissymmetry factor  $g$  of Type-II C line is only slightly larger than that under the excitation of a circularly polarized plane wave and is smaller than that of the Type-I C line in Fig. 2(c). This distinguishes the two types of C lines in terms of the ability of chiral discrimination. The different ability of chiral discrimination could be attributed to the fact that the Type-II C line is solely contributed by the electric dipole field of the gold sphere, while the Type-I C lines is also contributed by higher-order multipoles (i.e., magnetic dipole and electric quadrupole).

We analytically calculated the amplitudes of the electric and magnetic dipole moments induced in the helices at the considered positions of the Type-II C line. The results are shown in Fig. 5(a) and (b), where the blue lines denote the results of the LH helix and red dashed line denotes the results of the RH helix. Similar to the previous case, the dipoles of the LH and RH helices are symmetric with respect to the center position 6, while the dipoles of individual helix are asymmetric due to the chirality of the particle. In addition, the electric and magnetic dipoles show similar trend. Using Eq. (6) and (7), we analytically calculate the absorption and dissymmetry factor. The result is shown in Fig. 5(c) as the solid line. We notice that the analytical result well agrees with the full-wave numerical result (symbol line). This again demonstrates the validity of the multipole expansions method.

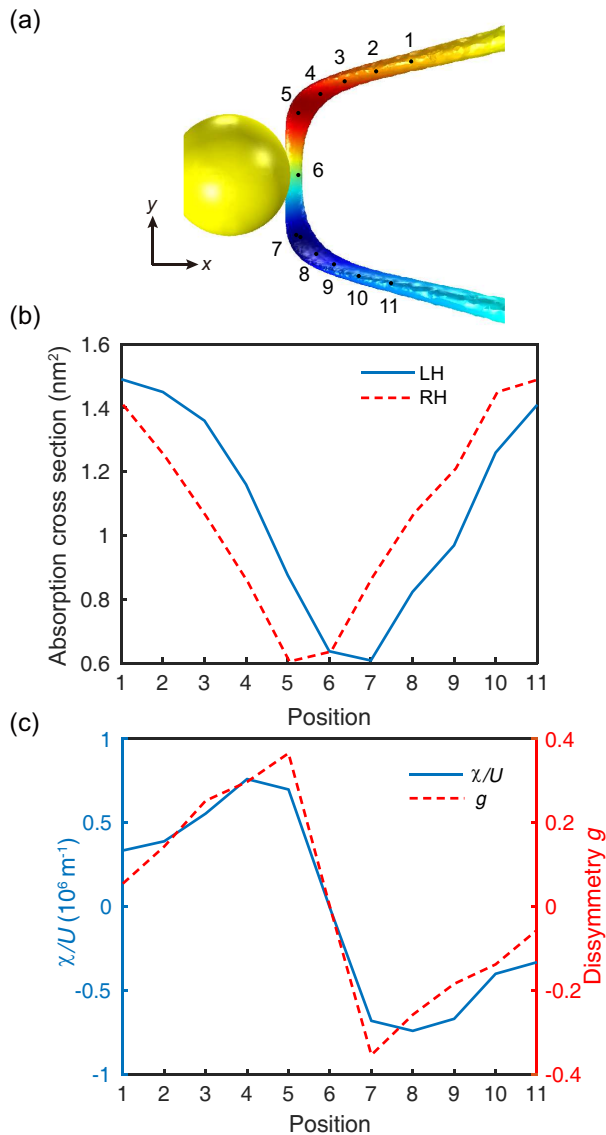


FIG. 4. (a) Schematic for chiral discrimination by the Type-II C line. (b) The absorption cross section of the LH (blue line) and RH (red line) helices as a function of the position. (c) The dissymmetry factor (blue line) and the normalized optical chirality (red line) as a function of the helix's position.

## V. CONCLUSION

In conclusion, we propose a new method to detect chiral particles by using the C lines of a gold sphere excited by linearly polarized light. By using full-wave numerical simulations and analytical multipole expansions, we studied the absorption of LH and RH gold helices locating at two types of C lines. We showed that the C lines can give rise to larger dissymmetry factor of absorption compared to normal plane waves of circular polarization. Importantly, we found that the multipole origin of the C lines can affect the dissymmetry factor and thus the

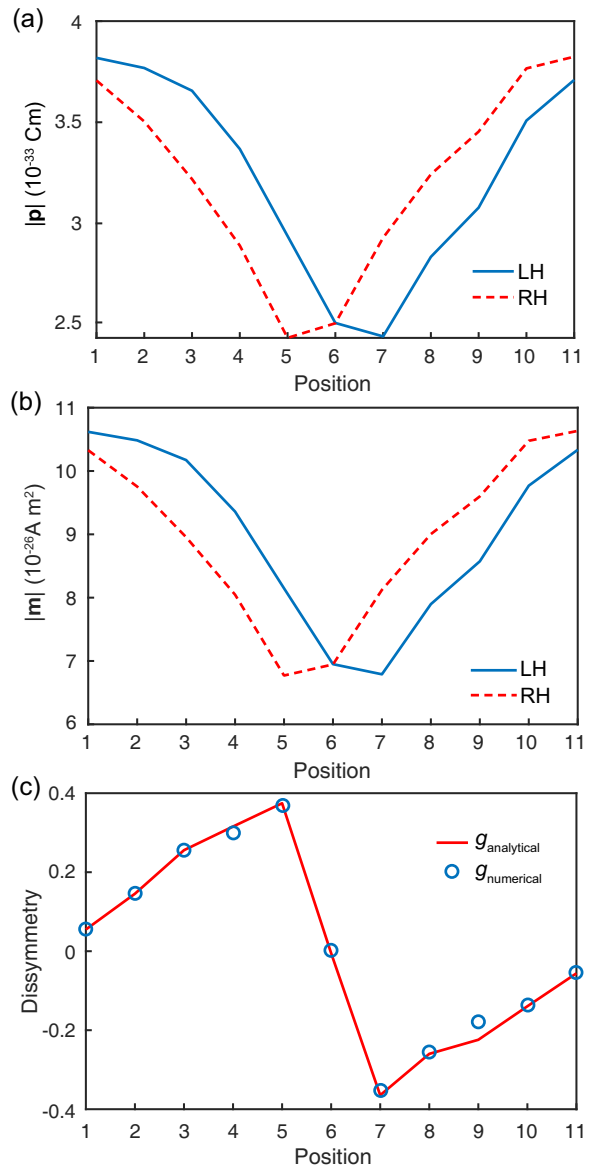


FIG. 5. Amplitude of (a) the electric dipole moment  $\mathbf{p}$  and (b) the magnetic dipole moment  $\mathbf{m}$  of the helices as a function of the position for the Type-II C line. (c) Comparison between the analytical (solid line) and numerical (symbol line) results of the dissymmetry factor.

ability of chiral discrimination. The C lines with higher-order multipoles can give rise to larger dissymmetry factor compared to the C lines dominated by electric dipole. By treating the helix particles as electric and magnetic dipoles, we uncover the interaction of the chiral particles with the C lines and its contribution to the absorption dissymmetry. The electric and magnetic dipoles have different amplitudes for the LH and RH helices, which account for their different absorption properties. The dissymmetry factor is proportional to the optical chirality of the C lines normalized by the total field energy density.

Our study provides a new method for chiral discrimination without using chiral excitations or chiral structures. Since a metal sphere is one of the simplest structures in nano fabrications, the proposed method should be easier to implement compared to previous proposals that involve complex structures and delicate designs. The results can generate novel applications in optical sensing, optical manipulations, and chiral quantum optics.

## VI. ACKNOWLEDGEMENTS

The work described in this paper was supported by grants from the Research Grants Council of the Hong Kong Special Administrative Region, China (Project No. CityU 11306019) and the National Natural Science Foundation of China (Project No. 11904306) .

- 
- [1] L. D. Barron, *Molecular Light Scattering and Optical Activity* [23] E. Hendry, T. Carpy, J. Johnston, M. Popland, R. V. Mikhaylovskiy, A. J. Laphorn, S. M. Kelly, L. D. Barron, N. Gadegaard, and M. Kadodwala, *Nat. Nanotechnol.* **5**, 783 (2010).
- [2] P. Melchiorre, M. Marigo, A. Carlone, and G. Bartoli, *Angew. Chem. Int. Ed* **47**, 6138 (2008).
- [3] S. B. Wang and C. T. Chan, *Nat. Commun.* **5**, 3307 (2014).
- [4] X.-L. Zhang, S. B. Wang, Z. Lin, H.-B. Sun, and C. T. Chan, *Phys. Rev. A* **92**, 043804 (2015).
- [5] J. Chen, S. Wang, X. Li, and J. Ng, *Opt. Express* **26**, 27694 (2018).
- [6] J. Pan, J.-H. Wu, H. Zhang, X. Ren, J.-P. Tan, L. Zhu, H.-S. Zhang, C. Jiang, and T. Wang, *Angew. Chem. Int. Ed* **58**, 7425 (2019).
- [7] K. J. Wo, J. Peng, M. K. Prasad, Y. Shi, J. Li, and S. Wang, *Phys. Rev. A* **102**, 043526 (2020).
- [8] M. D. Eastgate, M. A. Schmidt, and K. R. Fandrick, *Nat. Rev. Chem.* **1**, 1 (2017).
- [9] M. Suda, Y. Thathong, V. Promarak, H. Kojima, M. Nakamura, T. Shiraogawa, M. Ehara, and H. M. Yamamoto, *Nat. Commun.* **10**, 2455 (2019).
- [10] T. B. Freedman, X. Cao, R. K. Dukor, and L. A. Nafie, *Chirality* **15**, 743 (2003).
- [11] R. Tullius, A. S. Karimullah, M. Rodier, B. Fitzpatrick, N. Gadegaard, L. D. Barron, V. M. Rotello, G. Cooke, A. Laphorn, and M. Kadodwala, *J. Am. Chem. Soc.* **137**, 8380 (2015).
- [12] E. Vinegrad, D. Vestler, A. Ben-Moshe, A. R. Barnea, G. Markovich, and O. Cheshnovsky, *ACS Photon.* **5**, 2151 (2018).
- [13] E. A. Power and T. Thirunamachandran, *J. Chem. Phys.* **60**, 3695 (1974).
- [14] Y. Tang and A. E. Cohen, *Phys. Rev. Lett.* **104**, 163901 (2010).
- [15] L. Ye, L. Yang, X. Zheng, and S. Mukamel, *Phys. Rev. Lett.* **126**, 123001 (2021).
- [16] D. Patterson and J. M. Doyle, *Phys. Rev. Lett.* **111**, 023008 (2013).
- [17] A. O. Govorov, *J. Phys. Chem. C* **115**, 7914 (2011).
- [18] X. Zambrana-Puyalto, X. Vidal, and G. Molina-Terriza, *Nat. Commun.* **5**, 1 (2014).
- [19] C.-S. Ho, A. Garcia-Etxarri, Y. Zhao, and J. Dionne, *ACS Photon.* **4**, 197 (2017).
- [20] M. Hentschel, M. Schäferling, X. Duan, H. Giessen, and N. Liu, *Sci. Adv.* **3**, e1602735 (2017).
- [21] J. Lasa-Alonso, D. R. Abujetas, Á. Nodar, J. A. Dionne, J. J. Sáenz, G. Molina-Terriza, J. Aizpurua, and A. García-Etxarri, *ACS Photon.* **7**, 2978 (2020).
- [22] A. García-Etxarri, J. M. Ugalde, J. J. Sáenz, and V. Mujica, *J. Phys. Chem. C* **124**, 1560 (2020).
- [23] E. Hendry, T. Carpy, J. Johnston, M. Popland, R. V. Mikhaylovskiy, A. J. Laphorn, S. M. Kelly, L. D. Barron, N. Gadegaard, and M. Kadodwala, *Nat. Nanotechnol.* **5**, 783 (2010).
- [24] J. García-Guirado, M. Svedendahl, J. Puigdollers, and R. Quidant, *Nano Lett.* **18**, 6279 (2018).
- [25] E. Mohammadi, K. L. Tsakmakidis, A. N. Askarpour, P. Dehkhoda, A. Tavakoli, and H. Altug, *ACS Photon.* **5**, 2669 (2018).
- [26] M. V. Gorkunov, A. A. Antonov, and Y. S. Kivshar, *Phys. Rev. Lett.* **125**, 093903 (2020).
- [27] S. Beaulieu, A. Comby, D. Descamps, B. Fabre, G. A. Garcia, R. Géneaux, A. G. Harvey, F. Légaré, Z. Mašín, L. Nahon, A. F. Ordonez, S. Petit, B. Pons, Y. Mairesse, O. Smirnova, and V. Blanchet, *Nat. Phys.* **14**, 484 (2018).
- [28] J. F. Nye and J. V. Hajnal, *Proc. R. Soc. London A* **409**, 21 (1987).
- [29] M. R. Dennis, *Opt. Commun.* **213**, 201 (2002).
- [30] M. V. Berry, *J. Opt. A: Pure Appl. Opt.* **6**, 475 (2004).
- [31] I. Freund, *Opt. Commun.* **201**, 251 (2002).
- [32] M. V. Berry, *J. Opt. A: Pure Appl. Opt.* **6**, 675 (2004).
- [33] W. Chen, Q. Yang, Y. Chen, and W. Liu, *Phys. Rev. Lett.* **126**, 253901 (2021).
- [34] J. Peng, W. Liu, and S. Wang, *Phys. Rev. A* **103**, 023520 (2021).
- [35] A. Garcia-Etxarri, *ACS Photon.* **4**, 1159 (2017).
- [36] K. S. Grigoriev, N. Y. Kuznetsov, Y. V. Vladimirova, and V. A. Makarov, *Phys. Rev. A* **98**, 063805 (2018).
- [37] H. Larocque, D. Sugic, D. Mortimer, A. J. Taylor, R. Fickler, R. W. Boyd, M. R. Dennis, and E. Karimi, *Nat. Phys.* **14**, 1079 (2018).
- [38] D. Sugic and M. R. Dennis, *J. Opt. Soc. Am. A* **35**, 1987 (2018).
- [39] E. Pisanty, G. J. Machado, V. Vicuña-Hernández, A. Picón, A. Celi, J. P. Torres, and M. Lewenstein, *Nat. Photon.* **13**, 569 (2019).
- [40] N. Y. Kuznetsov, K. S. Grigoriev, Y. V. Vladimirova, , and V. A. Makarov, *Opt. Express* **28**, 27293 (2020).
- [41] R. L. Olmon, B. Slovick, T. W. Johnson, D. Shelton, S.-H. Oh, G. D. Boreman, and M. B. Raschke, *Phys. Rev. B* **86**, 235147 (2012).
- [42] www.comsol.com.
- [43] C. F. Bohren and D. R. Huffman, *Absorption and Scattering of Light by Small Particles*, 1st ed. (Wiley, New York, 1998).
- [44] J. D. Jackson, *Classical Electrodynamics*, 3rd ed. (Wiley, New York, 1998).
- [45] P. Grahn, A. Shevchenko, and M. Kaivola, *New J. Phys.* **14**, 093033 (2012).